Continuous monitoring of the isotopic composition of surface water vapor at Lhasa, southern Tibetan Plateau

Di Dai [a,d], Jing Gao [a,b,*], Hans Christian Steen-Larsen [c], Tandong Yao [a,b], Yaoming Ma [a,b], Meilin Zhu [a], Shenghai Li [a,b]

[a] *Key Laboratory of Tibetan Environment Changes and Land Surface Processes, Institute of Tibetan Plateau Research, Chinese Academy of Sciences, Beijing 100101, China*
[b] *CAS Center for Excellence in Tibetan Plateau Earth Sciences, Beijing 100101, China*
[c] *Geophysical Institute, University of Bergen, Bjerkness Centre for Climate Research, Bergen, Norway*
[d] *University of Chinese Academy of Sciences, Beijing 100049, China*

ARTICLE INFO

ABSTRACT

The stable isotopes (δ^{18}O and δD) of water vapor are used to characterize continuous variations in large-scale and boundary-layer atmospheric processes. We presented continuous measurements of δ^{18}O in surface water vapor at Lhasa, southern Tibetan Plateau, from October 2018 to September 2019 to investigate how large-scale and local atmospheric processes influence variations in water vapor δ^{18}O at different time scales. The water vapor δ^{18}O measurements reveal different seasonal characteristics and diurnal patterns. At the seasonal scale, δ^{18}O exhibits a W-shape with two maxima in May–June and October as well as two minima in July–August and February. The diurnal variations in the water vapor δ^{18}O and meteorological data throughout the year present distinct occurrences of maxima and minima during different periods. We found that the significant seasonal variability is mainly associated with the transition between the Indian summer monsoon and the westerlies, which transport distinct moisture to the southern Tibetan Plateau. The local temperature, specific humidity and boundary layer height impact the diurnal variations in water vapor δ^{18}O to some extent with remarkable seasonal differences.

1. Introduction

Stable isotopes in water contain abundant information for quantifying the hydrological cycle. Due to the differences in their saturation vapor pressures and molecular diffusivity, the relative abundances of stable isotopologues ($H_2^{16}O$, $HD^{16}O$ and $H_2^{18}O$) cause changes in hydrological processes (Barkan and Luz, 2007; Ellehoj et al., 2013; Majoube, 1971). Previous studies have documented that evaporation (Craig and Gordon, 1965; Merlivat and Jouzel, 1979), evapotranspiration (Farquhar et al., 2007), condensation (Ciais and Jouzel, 1994; Jouzel, 1986), and diffusion (Stewart, 1975) contained imprinted isotopic compositions of water.

Many studies have focused on precipitation stable isotopes over the Tibetan Plateau (TP) to understand the moisture transport and related moisture sources during the past 30 years. Previous studies have documented that seasonal changes in large-scale atmospheric circulations (the Indian summer monsoon and westerlies) resulted in the seasonality

of stable isotopes in precipitation (Yao et al., 2013; Yu et al., 2015a), and identified main moisture sources (Arabian Sea, Bay of Bengal and Mediterranean Sea, Gao et al., 2018). The isotopic compositions of Lhasa precipitation have shown the dominant influences of the Indian summer monsoon and westerlies, associated with intensive convection in the northern India along moisture transports depleting precipitation stable isotopes (Gao et al., 2013). The Indian summer monsoon and intensive convections result in low precipitation δ^{18}O normally, while the westerlies show relevant variations with high precipitation δ^{18}O. However, the relative impacts of large-scale circulation and local processes (e.g., rain evaporation and humidity effect) are not well known at diurnal and seasonal scales at Lhasa due to the inherent limitations of precipitation stable isotopes. Such effects are very important to evaluate the available moisture related with cloud formation and surface humidity.

Water vapor stable isotopes can reflect the continuous spatiotemporal variations in atmospheric processes. The earliest sampling of atmospheric water vapor stable isotopes was completed in the late 1950s.

Taylor (1968) analyzed deuterium in water vapor from the surface to a 5000-m height. White and Gedzelman (1984) found a positive correlation between water vapor δD and relative humidity/specific humidity. In the 1980s, a comprehensive sampling program measuring ^{2}H, ^{18}O, and ^{3}H in surface atmospheric water vapor in Paris, Hannover, Heidelberg, Krakow, and Miami found a relationship between variations in stable isotopes in water vapor and monthly averaged air temperatures (Schoch-Fischer et al., 1984). Gat et al. (2003) revealed that the isotope compositions of water vapor over the Mediterranean were affected by strong air-sea interactions, and the high d-excess (d-excess = δD-8*δ^{18}O) values were related to low humidity. Recently, continuous measurements of surface water vapor stable isotopes on Reunion Island (Guilpart et al., 2017), Siberia (Bastrikov et al., 2014), the Greenland ice sheet (Bonne et al., 2014; Steen-Larsen et al., 2013), and eastern China (Li et al., 2020; Wen et al., 2010) have revealed the dominant impact of local atmospheric humidity at diurnal and intraseasonal scales. Many studies have also identified the impacts of moisture sources and atmospheric processes during transport (Bonne et al., 2015; Laskar et al., 2014; Risi et al., 2013; Steen-Larsen et al., 2013, 2014). Yu et al. (2006, 2015b), Yin et al. (2008) and Tian et al. (2020) sampled stable isotopes in surface water vapor with cold traps in Nagqu, Delingha and Lhasa, respectively. They all noted that the distinct moisture sources of the Indian monsoon and the westerlies had significant impacts on the water vapor isotopes. In addition, precipitation processes during the monsoon period also affect the fluctuations of water vapor stable isotopes. Huang and Wen (2014) measured the in situ δ^{18}O, δD and d-excess values of atmospheric water vapor based on Picarro L1102i measurements and a matching calibration system from 27 May to 22 September 2012 in the Heihe River Basin. The marked diurnal cycle pointed to the influence of entrainment, local evapotranspiration (ET), and dewfall. However, no continued diurnal cycle of atmospheric water vapor stable isotopes in the TP has been reported thus far.

To accurately evaluate impacts of large-scale circulations and local processes on surface atmospheric water vapor at diurnal and seasonal scales, here, we presented high-resolution and continuous measurements of water vapor δ^{18}O using wave-length scanned-cavity ring down spectroscopy (WS-CRDS) from 1 October 2018 to 30 September 2019 at Lhasa. The goal of this paper is to detect the evolution of diurnal water vapor stable isotopes and to understand the influence of moisture sources and local surface processes on such evolution in the southern TP. Our results provide useful data to evaluate isotopic simulations from models and processes with an understanding of parameterization.

2. Materials and Methods

2.1. Water vapor isotope monitoring

The water vapor isotopic monitoring station of Lhasa (29.65°N, 91.03°E), southern TP, located on the north bank of the Lhasa River, a tributary of the Yarlung Zangbo River (Fig. 1), was established in summer 2014. The Indian monsoon controls summer moisture transport in this region, and approximately 85% of precipitation occurs in summer (Gao et al., 2013). The annual precipitation amounts during 2017–2019 were 412 mm, 322 mm and 318 mm, and the average annual air temperatures were 11.1 °C, 10.6 °C and 11.0 °C, respectively. Northeast winds prevail year round near the surface, and east-southwest winds account for 20% of the winds. Compared with annual precipitation amount at Lhasa during the past 30 years, the mean precipitation amount during our study duration is close to 30-yr mean value with a slight wet divergence (~7 mm).

The water vapor concentrations and isotopic compositions were measured using Picarro laser spectrometers L2130-i combined with an automatic calibration system using the Picarro standards delivery module (SDM) and vaporization module. The analyzer was set up in the attic of a four-story building with the inlet approximately 17 m above the ground. Ambient air was sampled through a 10-m-long, ¼-inch-
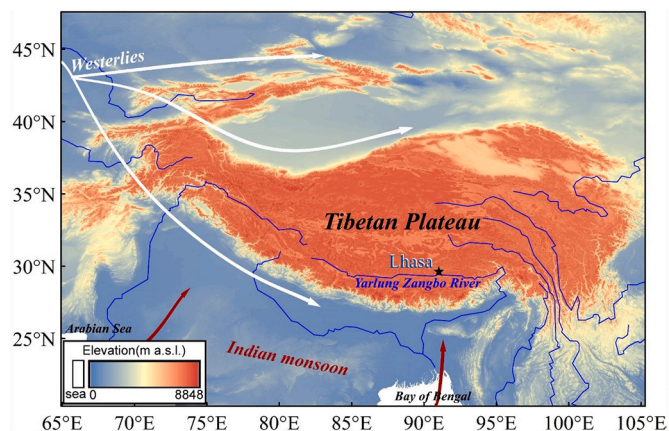

Fig. 1. Location of the Lhasa station (star) and schematic representation of the moisture transport by the westerlies and Indian summer monsoon over the Tibetan Plateau.

diameter Swagelok steel tube with a 5 L min^{-1} flow rate. The tube was temperature-autoregulated (at ~50 °C) to prevent condensation.

High-frequency (approximately 1 Hz) measurements were obtained during our monitoring period, and hourly/daily averages were analyzed in this study. Calibration is crucial for acquiring valid water vapor stable isotope measurements against the international IAEA VSMOW2-SLAP (Vienna Standard Mean Ocean Water-Standard Light Antarctic Precipitation). The in-situ measurements could be affected by internal and external factors, such as the humidity dependency and differences in the properties of each analyzer (Benetti et al., 2014; Schmidt et al., 2010). Steen-Larsen et al. (2013) established a rigorous calibration protocol that has been widely used for analyses of water vapor stable isotopes (Bastrikov et al., 2014; Bonne et al., 2014; Galewsky et al.,2016; Gu et al., 2019). The detailed calculation method used here is similar to that used in Steen-Larsen et al. (2013). Two water standards were injected by SDM in the vaporizer at 140 °C and measured by the analyzer. During the 1-year monitoring period, three water standards with δ^{18}O and δD values ranging from −42‰ to −10‰ and −334‰ to −70‰ were used for the calibration (Fig. S1), depending on the water vapor stable isotopic values. To assess the humidity-isotope response function, two standards were measured with 12–18 humidity levels from 1000 to 20,000 ppmv (Fig. S2) each month. The measured standard values were corrected using the humidity response function to the actual air humidity level with accuracies of 0.26‰ for δ^{18}O and 0.92‰ for δD; then, a linear regression was computed against the true values of both standards for each isotope. All measurements were calibrated before analysis was conducted with other data. In this study, isotopic measurements are reported relative to Vienna Standard Mean Ocean Water (VSMOW2) in per mil (‰) using δ-notation for the isotopic ratios, defined as a deviation of the sample isotopic ratio R$_{sample}$ compared to a standard isotopic ratio R$_{VSMOW}$:

$$\delta^{18}O = \left(R_{sample}/R_{VSMOW2}-1\right) \times 1000‰$$

Here, we used water vapor isotopic measurements collected from 1 October 2018 to 30 September 2019. Ambient humidity during the winter and spring periods appeared below 3000 ppmv frequently, which imparts an uncertainty to these measurements due to the large bias of standard measurements, although humidity levels of standards were measured between 1000 and 3000 ppmv in calibrations. The bias of standard measured below 3000 ppmv were twice larger than that of standard measured above 3000 ppmv, associated with large magnitudes of the isotopic variations. No drift effect was removed in calibrations. Two measurement gaps occurred from 13 November 2018 to 31 December 2018 and from 17 to 26 August 2019 due to problems with the calibration system. We validated measurements over 297 days,

approximately 81% of the total number of measured days.

2.2. Meteorological data

An automatic meteorological station (CR800 Series, Situated 1.8 m above ground) was installed 10 m from the inlets of the laser spectrometers. Temperature and relative humidity were measured by a humidity and temperature probe HMP155A (± 0.2 °C), wind direction and speed were measured by a Young 05103 sensor ($\pm 5°$; ± 0.3 m/s), pressure was measured by a PTB210 (± 0.5 hPa) and the precipitation amount was measured by a T-200B (± 0.6 mm). The air temperature, relative humidity, air pressure, wind speed, wind direction and precipitation amount were measured simultaneously with a 1-min temporal resolution. Hourly and daily averages are used in this study.

The humidity and temperature data measured by the automatic meteorological station were used to calculate the water vapor molar mixing ratio for comparison with the water vapor mixing ratio measured by Picarro (Fig. S3). The datasets show a significant linear correlation: y = 1.04x-32.19, ($R^2 = 0.99$, $n = 6639$), where x denotes the Picarro mixing ratio and y denotes the automatic meteorological mixing ratio, confirming the reliability of the data. Bastrikov et al. (2014) and Aemisegger et al. (2012) also showed a linear response relationship despite the different calibration units. Bonne et al. (2014) and Tremoy et al. (2011), however, showed a nonlinear response of the analyzers compared to independent meteorological device observations. The humidity data analyzed in this study were averaged using meteorological measurements.

Hourly boundary layer height (BLH) data with a 0.25° × 0.25°

resolution were downloaded from the European Centre for Medium-Range Weather Forecasts (ECMWF) reanalysis dataset (ERA5) (Hersbach et al., 2018) to probe the variation in the boundary layer.

2.3. HYSPLIT model calculation

The HYSPLIT (Hybrid Single Particle Lagrangian Integrated Trajectory) model was used to identify the moisture transport paths (Stein et al., 2015) with the Global Data Assimilation System (GDAS) dataset at 1° × 1° and 3-h spatial and temporal resolutions (Kleist et al., 2009). Because most atmospheric water vapor is distributed 0–2 km above ground level (Wallace and Hobbs, 2006), the initiated heights for the back trajectory are 100 m above the ground in this study. The daily moisture trajectories during the sampling period (1 October 2018 to 30 September 2019) were calculated for 5 days prior to the sampling date (Gao et al., 2013) at Lhasa. Then, the daily trajectories were clustered in the premonsoon, monsoon, postmonsoon and winter periods by using the built-in cluster analysis mode (Borge et al., 2007). The corresponding daily water vapor isotopic values were averaged as the clustered seasonal values.

3. Results

3.1. Seasonal variability and statistical relationships with local climate

The daily averaged measurements of water vapor δ^{18}O, δD, the corresponding air temperature, the specific humidity and the precipitation amount over the monitoring period are presented in Fig. 2. The air
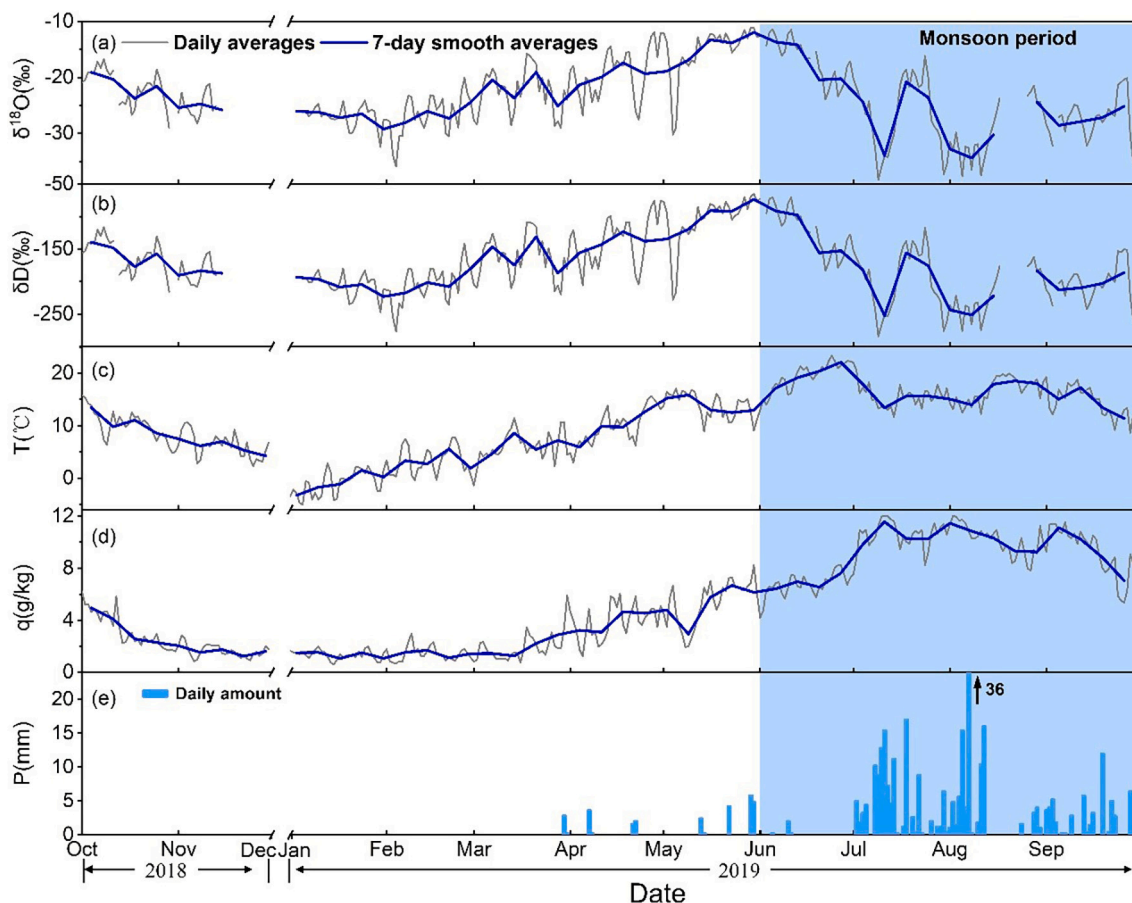
Fig. 2. Daily measurement time series obtained at Lhasa from the Picarro instrument and the corresponding meteorological data from 1 October 2018 to 30 September 2019. The gray and blue lines are the daily averages and 7-day smooth averages, respectively. Top to bottom panels: (a) δ^{18}O (‰), (b) δD (‰), (c) air temperature (°C), (d) specific humidity (g/kg) and (e) daily precipitation amount (mm). The blue shadow indicates the monsoon period. (For interpretation of the references to colour in this figure legend, the reader is referred to the web version of this article.)

temperature, specific humidity and precipitation amount show clear unimodal seasonal variabilities with high values in July–September and low values in January–March. In contrast, $\delta^{18}O$ shows W-shaped seasonal variability with two maxima in May–June (−15.2‰) and October (−21.6‰) and two minima in July–August (−29.8‰) and February (−26.7‰), which is consistent with results from Tian et al., (2020) with ~13‰ larger $\delta^{18}O$ amplitudes. A seasonal amplitude of 7.8‰ was obtained for $\delta^{18}O$ and of 69.8‰ for δD. The $\delta^{18}O$ and δD values in July-–August are approximately 12‰ and 150‰, lower than those in May–June. From October to February, $\delta^{18}O$ decreases gradually from the maximum in October to minimum in February, in phase with specific humidity (q). Since March, water vapor $\delta^{18}O$ enriched till the beginning of June, consistent with the linear warming. After June, water vapor $\delta^{18}O$ drops rapidly till the minimum in the beginning of July, then a peak was observed in the mid of July and decreased again in August, which are almost reversed with variations of simultaneous q. In contrast, shifts of water vapor $\delta^{18}O$ are homodromous with that of temperature from the late June to the mid of August. The high precipitation amounts in July and August are associated with two valleys of water vapor $\delta^{18}O$, indicated the possible impact of precipitation events. δD shows similar variations to those of $\delta^{18}O$ ($R^2 = 0.98$, $P < 0.01$) due to equilibrium processes. The seasonal pattern of precipitation $\delta^{18}O$ also shows the maximum in May and minimum in August, but without the remarkable second extrema (Gao et al., 2013, 2018). Such seasonal variability is associated with the transition between the Indian summer monsoon and the westerlies (Yao et al., 2013; Gao et al., 2013). The Indian monsoon brings warm and wet moisture from the Bay of Bengal and Arabian Sea as well as the tropical Indian Ocean to the TP, resulting in the manifested depletion of water vapor and precipitation $\delta^{18}O$ (Tian et al., 2001, 2020; Yu et al., 2015a, 2015b), while enrichments in $\delta^{18}O$ are exhibited during the premonsoon and postmonsoon periods. Following previous studies (e.g., Gao et al., 2018), the values obtained from 1 June to 30 September during our observation period were selected to reflect the diurnal variability dominated by the Indian summer monsoon. The October–November period is considered the postmonsoon period, December–February is considered the winter period, and the other months are considered the premonsoon period. However, such W-shape seasonal variability is different from that in the regions dominated by the westerlies. Yu (2016) found enriched water vapor $\delta^{18}O$ in June-–August and ~15‰ depletion in December–February at Taxkorgan, the northern TP, where the westerlies are the dominate circulation all year round. Bastrikov et al. (2014) depicted the maximum isotopes in August and minimum in January at Kourovka, western Siberia, and such

seasonal pattern is parallel with that of humidity and temperature. As shown in Table 1, the mean $\delta^{18}O$ (−23.2‰) is consistent with previous observations at Lhasa (−23.1‰) by the cryogenic trapping method (Tian et al., 2020), which is much depleted compared with that at Zhangye (−14.9‰) (Huang and Wen, 2014) and Delingha (−21.2‰) (Yin et al., 2008). Such spatial distinctions in water vapor $\delta^{18}O$ at these three stations are consistent with precipitation $\delta^{18}O$ (Yao et al., 2013), resulting from the spatial influence of the Indian summer monsoon. Further analysis of the dominant influence between the Indian summer monsoon and the westerlies will be discussed in detail in Section 3.3.

Seasonality is also presented in water vapor $\delta^{18}O$-δD patterns (Fig. 3). The daily averaged $\delta^{18}O$ and δD over our observation period show a slope of 8.04 ($n = 297$, $R^2 = 0.98$), similar to the GMWL, but with a high intercept of 15.52 (Table 1). The maximum slope (8.27) and intercept (21.88) are found in the premonsoon period, and the minima (7.63 for slope and 5. 78 for intercept) are found under the monsoon

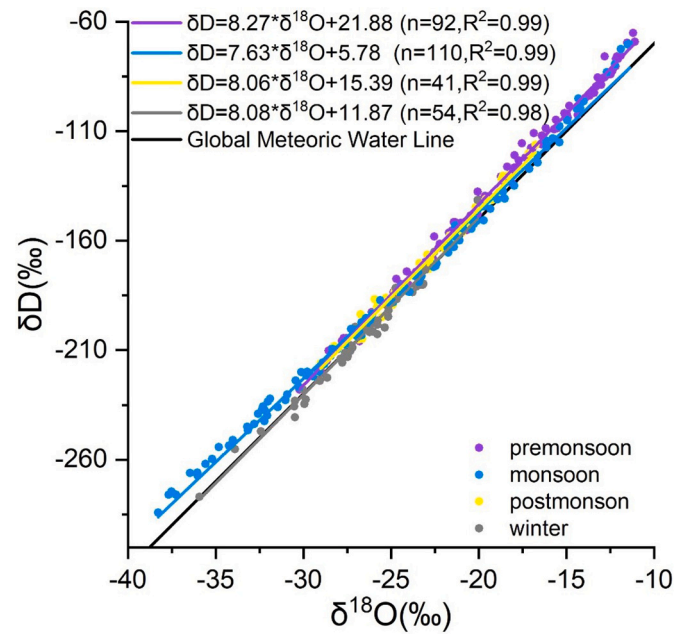**Fig. 3.** The local water vapor lines (LWVLs) at Lhasa during the four periods of study. The dots show the daily averaged $\delta^{18}O$ and δD values.

Table 1

Statistics of air temperature (T), specific humidity (q), precipitation amount (P), $\delta^{18}O$ and δD from 1 October 2018 to 30 September 2019 based on daily averages (sums of the precipitation variables) on monthly, seasonal and annual scales. The slopes and intercepts of the local water vapor lines were computed only on seasonal and annual scales. The mean temperature, specific humidity and the accumulated precipitation values and the appended variable coefficient (CV) values for water vapor isotopes ($\delta^{18}O$ and δD) are shown.

| Date	T	P	q	$\delta^{18}O$		δD		Slope	Intercept
	°C	mm	g/kg	mean ± σ	CV	mean ± σ	CV		
All	10.4	318.2	5.1	−23.2 ± 6.1	0.27	−170.8 ± 49.6	0.29	8.04	15.52
Postmonsoon	8.3	0.0	2.5	−22.7 ± 3.2	0.14	−167.2 ± 26.2	0.16	8.06	15.39
Winter	1.0	0.0	1.4	−26.8 ± 2.9	0.11	−204.7 ± 23.6	0.12	8.08	11.87
Premonsoon	9.9	27.8	3.7	−19.0 ± 5.2	0.27	−134.9 ± 42.6	0.32	8.27	21.88
Monsoon	16.5	290.4	9.2	−25.1 ± 6.9	0.27	−185.5 ± 52.5	0.28	7.63	5.78
Oct-18	10.2	0.0	3.3	−21.6 ± 3.1	0.14	−158.5 ± 24.9	0.16	–	–
Nov-18	6.3	0.0	1.6	−25.0 ± 2.2	0.09	−186.1 ± 18.0	0.10	–	–
Jan-19	−1.0	0.0	1.3	−26.9 ± 1.9	0.07	−205.2 ± 16.5	0.08	–	–
Feb-19	3.4	0.0	1.4	−26.7 ± 3.6	0.14	−204.2 ± 29.0	0.14	–	–
Mar-19	6.0	3.0	1.9	−22.5 ± 3.8	0.17	−163.3 ± 32.3	0.20	–	–
Apr-19	9.8	7.4	3.9	−19.2 ± 4.3	0.22	−137.5 ± 36.3	0.26	–	–
May-19	13.9	17.4	5.4	−15.2 ± 4.4	0.29	−103.9 ± 37.0	0.36	–	–
Jun-19	19.3	2.4	6.7	−16.8 ± 3.7	0.22	−121.5 ± 34.1	0.28	–	–
Jul-19	15.7	126.2	10.5	−26.5 ± 6.4	0.24	−197.3 ± 47.4	0.24	–	–
Aug-19	16.7	106.4	10.2	−29.8 ± 4.9	0.17	−220.3 ± 34.4	0.16	–	–
Sep-19	14.4	55.40	9.3	−27.5 ± 3.9	0.14	−204.9 ± 30.0	0.14	–	–

influence. Such characteristics reflect strong evaporation during the premonsoon period, moisture originating from wettest sources during the monsoon period and driest sources during the premonsoon period (Gao et al., 2013; He et al., 2015; Risi et al., 2013).

The seasonality is also imprinted in correlations between daily water vapor $\delta^{18}O$ and local meteorological conditions (Fig. 4). Significantly positive correlations between daily $\delta^{18}O$ and surface air temperature are observed during monsoon ($R^2 = 0.25$, slope = 1.1‰°C^{-1}), premonsoon ($R^2 = 0.24$, slope = 0.6‰°C^{-1}) and postmonsoon ($R^2 = 0.14$, slope = 0.4‰°C^{-1}) periods. In addition, surface specific humidity is positively correlated with daily $\delta^{18}O$ during nonmonsoon periods (Fig. 4) and vice versa during the monsoon period, similar to the results of Tian et al. (2020). A negative correlation with the precipitation amount ($R^2 = 0.17$, slope = -0.6‰ mm^{-1}) is also observed during the monsoon period.

3.2. Diurnal variability and statistical relationships with local climate

Clear diurnal cycles were observed in the stable isotopes of water vapor (Fig. 5). To exhibit the seasonal variations in these diurnal cycles, different cases are depicted here. The air temperature and boundary layer height (BLH) show consistent diurnal cycles throughout the year, with maxima measured during 14:00–15:00 local time (LT) and minima measured during 6:00–7:00 LT. Amplitudes of 9 °C in air temperature, 1.8 g/kg in specific humidity and 1800 m in BLH were obtained during the monsoon period. The air temperature amplitudes measured during

the pre- and postmonsoon periods are slightly larger (approximately 2 °C larger) than that measured during the monsoon period, while a difference of more than 2000 m is shown in the BLH amplitudes between the winter and premonsoon periods. Specific humidity shows antiphase activity with air temperature with a much smaller amplitude of 0.7 g/kg in winter. Precipitation mainly occurred during the monsoon period, accounting for ~88% of the annual accumulation, and ~10% of the annual precipitation occurred during the premonsoon period with very small hourly average (Fig. 5a). However, $\delta^{18}O$ exhibited different diurnal cycles between the monsoon and nonmonsoon (including premonsoon, postmonsoon and winter) periods. During the monsoon period, the minimum $\delta^{18}O$ was observed at 8:00 LT and the maximum at 19:00 LT with an amplitude of approximately 2‰, and the diurnal $\delta^{18}O$ variations showed significant positive correlations with specific humidity and air temperature except around sunset (Fig. S4). During nonmonsoon periods, the minimum $\delta^{18}O$ was observed at 16:00 LT and the maximum at 7:00–9:00 LT, with the largest amplitude of approximately 5‰ observed in winter, and the diurnal $\delta^{18}O$ variations were positively correlated with the specific humidity throughout the day (Fig. S4). The manifested second $\delta^{18}O$ minimum was observed at 6:00 LT during the postmonsoon period, associated with the minimum air temperature. During the pre- and postmonsoon periods, the air temperature showed opposite correlations with the water vapor $\delta^{18}O$ in the daytime and nighttime, but this positive correlation disappeared in the daytime in winter. A similar diurnal cycle of water vapor $\delta^{18}O$ was observed
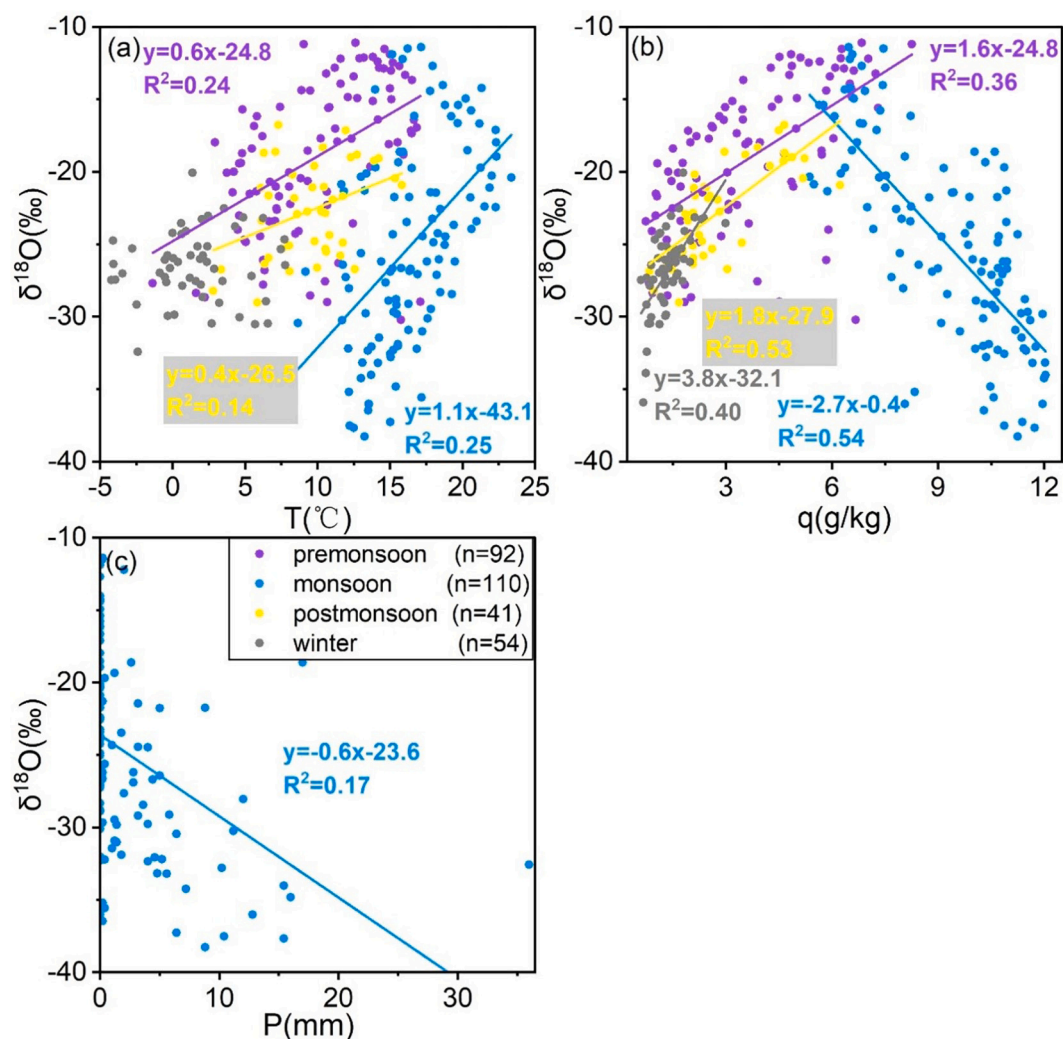
Fig. 4. Linear regressions. (a) $\delta^{18}O$ vs. T, (b) $\delta^{18}O$ vs. q, and (c) $\delta^{18}O$ vs. P, based on daily values. The linear regression curves in the plot all met the 95% significance test.
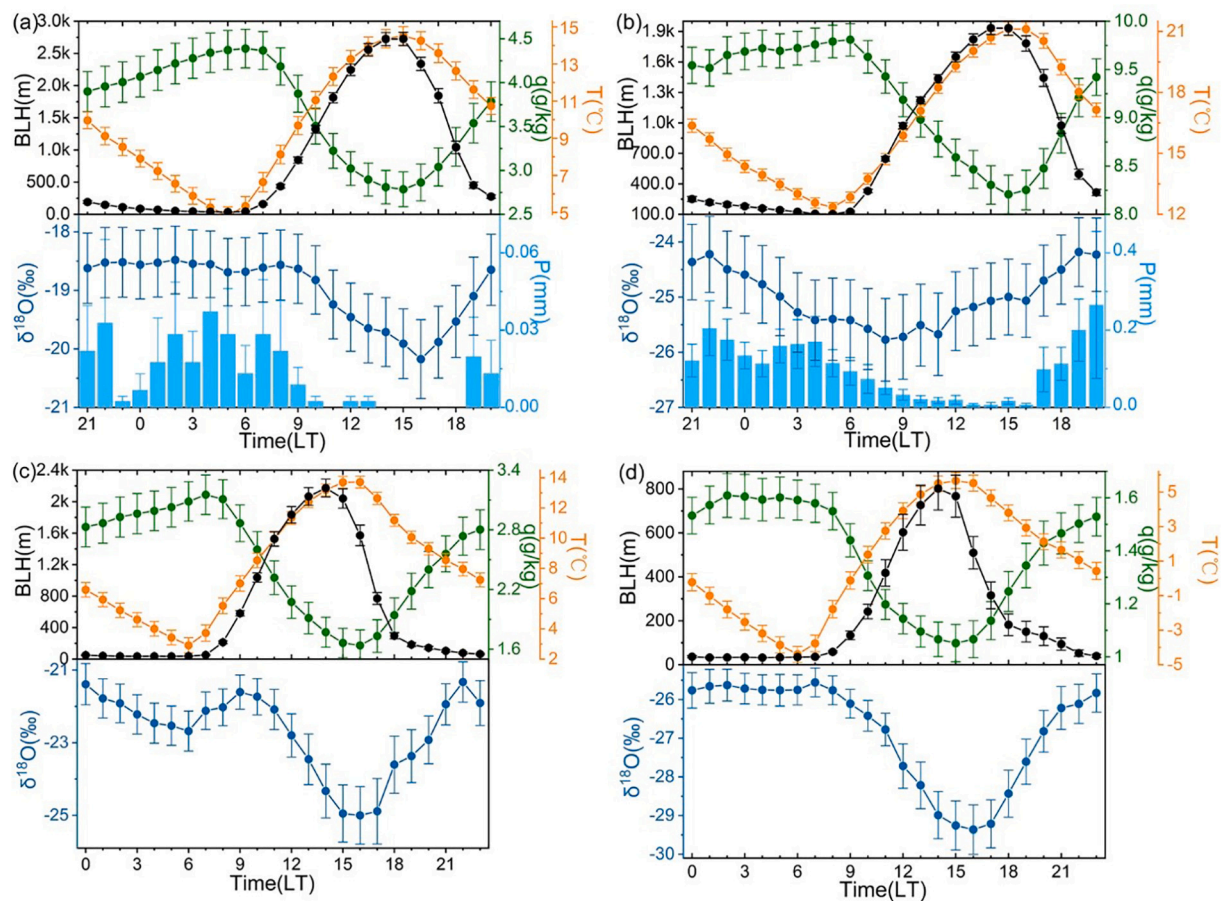
Fig. 5. The mean diurnal cycles of T, q, the boundary layer height (BLH), δ¹⁸O and P (the hourly precipitation average, plotted only for the monsoon season) during the (a) premonsoon, (b) monsoon, (c) postmonsoon and (d) winter periods. The error bars show the standard errors of the data, calculated hourly. Please notice the different Y-axis for precipitation amount.

during the monsoon period at the NEEM surface by Steen-Larsen et al. (2013), and the amplitude of the δ¹⁸O diurnal cycle at Lhasa was larger than that at Ivittuut, southern Greenland (Bonne et al., 2014). These studies in Greenland suggested that such diurnal variability in water vapor stable isotopes was attributed to exchanges of humidity between air and snow surfaces and the influence of the advection of marine moisture. In our case, the large-scale advection (e.g., Indian summer monsoon) is attributed to seasonal variations in the δ¹⁸O diurnal cycle, whereas local air temperature and specific humidity as well as the BLH impact variations in the δ¹⁸O diurnal cycle. The BLH only showed negative correlations with δ¹⁸O in the daytime without the influence of monsoons. At midday with a large BLH, the effects of air temperature and specific humidity were also stronger than those measured at night during the nonmonsoon periods (Fig. S4), indicating the effect of surface turbulence (Lai et al., 2006; Welp et al., 2008; Zhang et al., 2011) and local evapotranspiration. However, the monsoon overwhelmed the effect of surface turbulence to some extent. The diurnal characteristic of the δ¹⁸O may related with the diurnal variations of the sunrise and sunset during the monsoon period. In the day time, the temperature and humidity increase after sunrise with the accumulation of surface energy and intensifying of local evapotranspiration, associated with enrichment of the δ¹⁸O, verse vice in the night.

To probe the possible influence of summer nocturnal precipitation on the diurnal water vapor δ¹⁸O, precipitation events with amounts larger than 10 mm on July 11–12 and August 7–8 are shown in the Fig. S5 due to missing the simultaneous precipitation stable isotopes. We found that temperature started to decrease about one hour ago, while the q and RH increased simultaneously. However, water vapor δ¹⁸O did not show

consistent variations with any of them. At 2 am of July 11–12 and 18 pm of August 7–8, the water vapor δ¹⁸O started to decrease slightly during changing of humidity and temperature. In contrary, the remarkable increase (~5‰) of water vapor δ¹⁸O was observed about one hour ago. With the accumulation of precipitation amount, water vapor δ¹⁸O kept enriching from 18 pm to 2 am, and then decreased rapidly by ~6‰ till 10 am after the sunrise on July 11–12, which fell behind the transition of the RH and q. However, rapid decreasing of water vapor δ¹⁸O by ~8‰ was observed since the precipitation occur on August 7–8, which was not parallel with variations of q, RH and temperature. These characteristics indicated the influence of summer nocturnal precipitation on the water vapor δ¹⁸O, which may result from overlapped influences of weather conditions.

### 3.3. Seasonal moisture sources diagnostic

Seasonal shifts in large-scale atmospheric circulations (the westerlies and Indian summer monsoon) result in varying moisture transport processes (Yao et al., 2013). Back-trajectories and specific humidity along the clustered trajectories were calculated during the four studied periods to diagnose seasonal moisture sources during our observation period (Fig. 6). The back-trajectories highlight seasonal shifts in moisture sources for Lhasa, potentially causing varying stable isotopes in the water vapor at Lhasa, which are consistent with results from previous studies on precipitation stable isotopes (Gao et al., 2013). During the premonsoon period, three sources were identified, including one in the southern Himalayas across Bhutan (71% of the total trajectories), one in the western TP (21% of the total trajectories), and one in Irian (8% of the
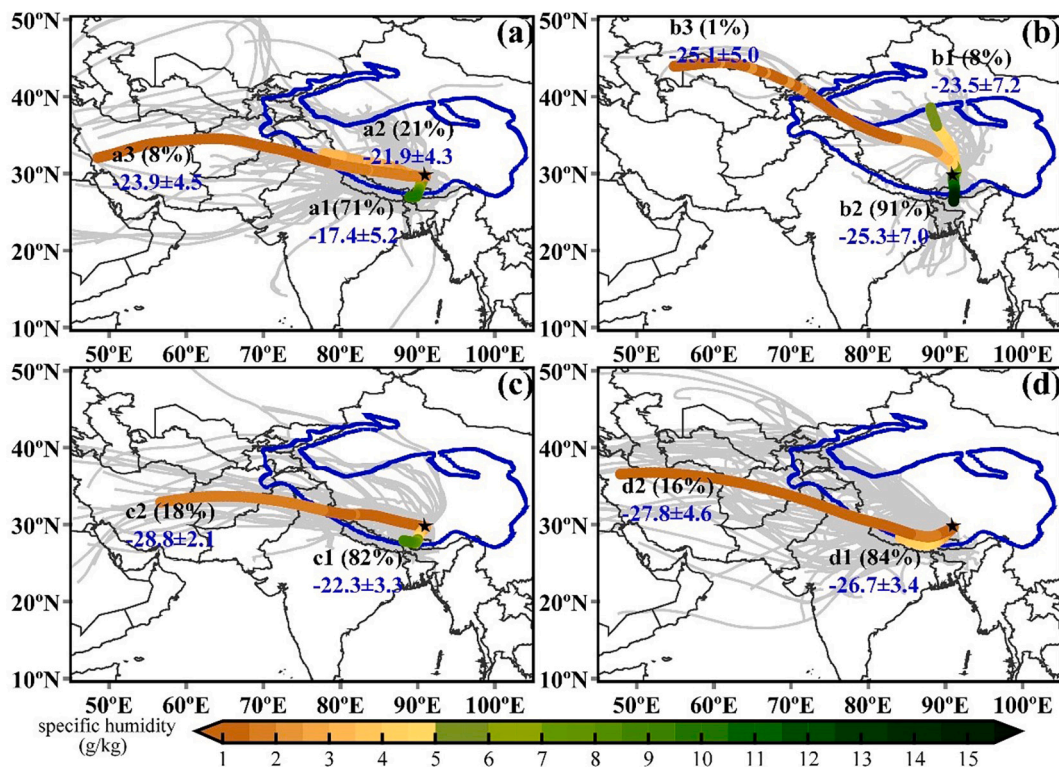
Fig. 6. Back trajectories calculated 120-h back using the HYSPLT model during the (a) premonsoon, (b) monsoon, (c) postmonsoon and (d) winter periods. The changes in specific humidity along each clustered trajectory are shown in colour. The black letters and numbers represent the name of each clustered trajectory, and the percentages indicate the proportion of each clustered trajectory. The blue numbers show the mean δ^{18}O (±1σ) value for each cluster. We calculated the 6-h δ^{18}O average corresponding to each daily trajectory separated by UTC 00:00, 06:00, 12:00 and 18:00, then calculated the average of those results for each cluster. (For interpretation of the references to colour in this figure legend, the reader is referred to the web version of this article.)

total trajectories). The source in the southern Himalayas across Bhutan contributed the main moisture source to Lhasa, associated with the highest average water vapor δ^{18}O (−17.4‰). The specific humidity values along the trajectories of the other two sources were lower than 3 g/kg, associated with low average water vapor δ^{18}O values (less than −21‰, Fig. 6a). During the monsoon period, the source in the southern Himalayas, which contributed dominant moisture to Lhasa (91% of the total trajectories) with a specific humidity greater than 9 g/kg, resulted in depleted water vapor δ^{18}O (−25.3‰). Such characteristics are consistent with variations in precipitation stable isotopes due to moisture controlled by the Indian summer monsoon (Gao et al., 2018). During the postmonsoon period (Fig. 6c), only two sources were clustered. The dominant source (82% to total trajectories), located in the southern TP along the Himalayas, transports moist air to Lhasa, and the other source in Irian transported comparatively less moisture overall. Such changes in moisture sources result in the enrichment of water vapor δ^{18}O by ~5‰. In winter (Fig. 6d), moisture transport controlled by the westerlies (Yao et al., 2013) brings dry air with a specific humidity less than 5 g/kg to Lhasa, associated with the lowest average water vapor δ^{18}O measured throughout the year.

We used q-δ^{18}O plots (Galewsky et al., 2016; Benetti et al., 2018) combined with theoretical Rayleigh distillation curves and mixing lines to assess the mixing situations during the four studied periods (Fig. 7). The theoretical Rayleigh curve was calculated with an initial δ^{18}O value of −9.3‰, which was equal to the evaporated δ^{18}O in equilibrium with ocean water at 25 °C (RH = 80%). The mixing curve is calculated with the dry source, which is represented by the driest measurements at Lhasa with a specific humidity of 0.5 g/kg and a δ^{18}O value of −40‰, and the wet source, which is equal to the initial condition for the theoretical Rayleigh curve. The moist measurements are partitioned from dry measurements in Fig. 7, which provides evidence of two-series distinct moisture mixing during the monsoon period and nonmonsoon periods,
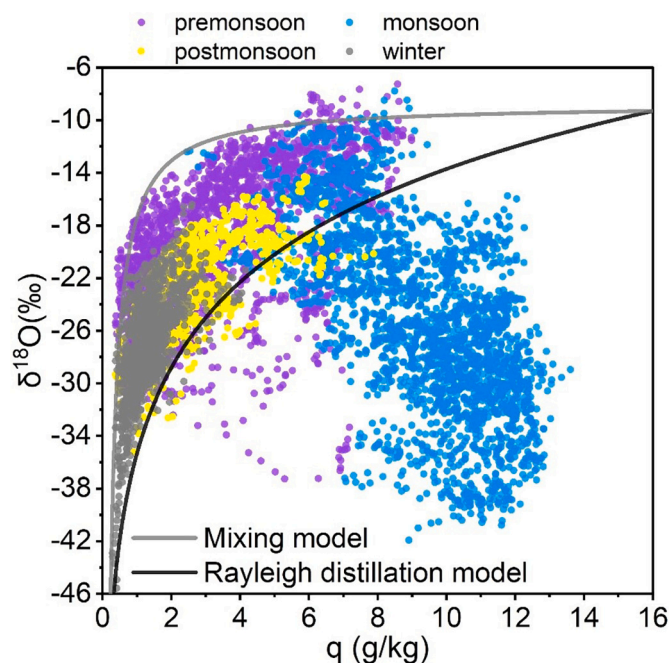
Fig. 7. Scatter plot of the observed hourly water vapor δ^{18}O vs. q. The solid black curve represents the Rayleigh distillation line calculated for the initial conditions of δ^{18}O = −9.3‰ (a value for water vapor in equilibrium with ocean water at T = 25 °C) and q = 16 g/kg (RH = 80%). The gray curve represents the mixing line that originates from the driest vapor at Lhasa when the vapor is evaporated from the ocean.

consistent with the characteristics of moisture transport described in Section 3.3. During the monsoon period, most measurements lie below the Rayleigh curve and are not described accurately by either the Rayleigh or binary mixing descriptions that we assumed. Such distributions are similar to the "amount effect" feature, which is found in precipitation $\delta^{18}O$ during large precipitation events and is often explained by the effect of evaporating rainfall near active convection (Worden et al., 2007). However, most of the measurements lie within these two descriptions during the premonsoon, monsoon and postmonsoon periods. A few datapoints lie on the Rayleigh curve, indicating the loss of isotopic depletion as vapor to precipitation. The few enriched datapoints above the mixing line may indicate vapor from local evapotranspiration. The overlapping distributions between the monsoon period and non-monsoon periods indicate the similar effects of evaporation and condensation on water vapor stable isotopes (Worden et al., 2007).

4. Conclusions

Here, we have presented a 1-year-long monitoring campaign of atmospheric water vapor $\delta^{18}O$ in Lhasa, southern TP. The accuracy and precision of the water vapor $\delta^{18}O$ measurements allow us to investigate the diurnal and seasonal impacts of large-scale atmospheric circulations and local processes on surface water vapor stable isotopes. We identified a W-shaped seasonal variability in water vapor $\delta^{18}O$ and distinct $\delta^{18}O$ diurnal cycles. The daily water vapor $\delta^{18}O$ showed a positive correlation with the air temperature in January–October and the opposite correlation with the specific humidity between the monsoon and nonmonsoon periods. We demonstrated that such characteristics are associated with shifts in the dominant large-scale atmospheric circulations (i.e., the westerlies and Indian summer monsoon). Local processes (e.g., the air temperature, specific humidity and BLH) act on water vapor $\delta^{18}O$ beneath large-scale atmospheric circulations, resulting in variable correlations at different time scales. Long-term surface water vapor monitoring at Lhasa is critically needed to diagnose the interannual variability. An important next step will be to probe the synoptic impacts on variations in water vapor $\delta^{18}O$ and test the performances of isotopic general circulation models (Steen-Larsen et al., 2017) and data retrievals based on remote sensing (Galewsky et al., 2016; Worden et al., 2007).

Declaration of Competing Interest

The authors declare that they have no known competing financial interests or personal relationships that could have appeared to influence the work reported in this paper.

Acknowledgments

Appendix A. Supplementary data

Supplementary data to this article can be found online at https://doi.org/10.1016/j.atmosres.2021.105827.

References

Aemisegger, F., et al., 2012. Measuring variations of $\delta^{18}O$ and δ^2H in atmospheric water vapour using two commercial laserbased spectrometers: an instrument characterisation study. Atmos. Meas. Tech. 5, 1491–1511. https://doi.org/10.5194/amt-5-1491-2012.

Barkan, E., Luz, B., 2007. Diffusivity fractionation of H216O/H217O and H216O/H218O in air and their implications for isotope hydrology. Rapid Commun. Mass Spectrom. 21, 2999–3005. https://doi.org/10.1002/rcm.3180.

Bastrikov, V., et al., 2014. Continuous measurements of atmospheric water vapour isotopes in western Siberia (Kourovka). Atmos. Meas. Tech. 2014, 7(6). https://doi.org/10.5194/amt-7-1763-2014.

Benetti, M., et al., 2014. Deuterium Excess in Marine Water Vapor: Dependency on Relative Humidity and Surface Wind Speed during Evaporation. IEEE International Conference on Image Processing. IEEE.

Benetti, M., et al., 2018. A framework to study mixing processes in the marine boundary layer using water vapor isotope measurements. Geophys. Res. Lett. 45, 2524–2532. https://doi.org/10.1002/2018GL077167.

Bonne, J.L., et al., 2014. The isotopic composition of water vapour and precipitation in Ivittuut, southern Greenland. Atmos. Chem. Phys. 14 https://doi.org/10.5194/acp-14-4419-2014, 4419–2014.

Bonne, J.L., et al., 2015. The summer 2012 Greenland heat wave: in situ and remote sensing observations of water vapor isotopic composition during an atmospheric river event. J. Geophys. Res. Atmos. 120 (7), 2970–2989. https://doi.org/10.1002/2014jd022602.

Borge, R., et al., 2007. Analysis of long-range transport influences on urban PM10 using two stage atmospheric trajectory clusters. Atmos. Environ. 41, 4434–4450. https://doi.org/10.1016/j.atmosenv.2007.01.053.

Ciais, P., Jouzel, J., 1994. Deuterium and oxygen 18 in precipitation: isotopic model, including mixed cloud processes. J. Geophys. Res. Atmos. 99, 16793–16803. https://doi.org/10.1029/94JD00412.

Craig, H., Gordon, L.I., 1965. Deuterium and oxygen-18 variations in the ocean and the marine atmosphere. In: Tongiorgi, E. (Ed.), Stable Isotopes in Oceanographic Studies and Paleotemperatures. V. Lishi e F, Pisa, Spoleto, Italy, pp. 9–130.

Ellehoj, M.D., et al., 2013. Ice-vapor equilibrium fractionation factor of hydrogen and oxygen isotopes: Experimental investigations and implications for stable water isotope studies. Rapid Commun. Mass Spectrom. 27 (19), 2149–2158. https://doi.org/10.1002/rcm.6668.

Farquhar, G.D., Cernusak, L.A., Barnes, B., 2007. Heavy water fractionation during transpiration. Plant Physiol. 143, 11–18. https://doi.org/10.1104/pp.106.093278.

Galewsky, J., et al., 2016. Stable isotopes in atmospheric water vapor and applications to the hydrologic cycle. Rev. Geophys. 54 (4), 809–865. https://doi.org/10.1002/2015rg000512.

Gao, J., et al., 2013. What controls precipitation ^{18}O in the southern Tibetan Plateau at seasonal and intra-seasonal scales? A case study at Lhasa and Nyalam. Tellus B. 65 https://doi.org/10.3402/tellusb.v65i0.

Gao, J., et al., 2018. ENSO Effects on Annual Variations of Summer Precipitation Stable Isotopes in Lhasa, Southern Tibetan Plateau. J. Clim. 31 (3), 1173–1182. https://doi.org/10.1175/JCLI-D-16-0868.1.

Gat, J.R., et al., 2003. Isotope composition of air moisture over the Mediterranean Sea: an index of the air-sea interaction pattern. Tellus B 55 (5), 953–965. https://doi.org/10.3402/tellusb.v55i5.16395.

Gu, X.Q., et al., 2019. Study on calibration method for atmospheric water vapor stable isotopes observed by cavity ring-down spectroscopy. Spectrosc. Spectr. Anal. 39 (6), 1700–1705. https://doi.org/10.3964/j.issn.1000-0593(2019)06-1700-06.

Guilpart, E., et al., 2017. The isotopic composition of near-surface water vapor at the Mado observatory (Reunion Island, southwestern Indian Ocean) documents the controls of the humidity of the subtropical troposphere. J. Geophys. Res. Atmos. doi. https://doi.org/10.1002/2017JD026791.

He, Y., et al., 2015. Impact of atmospheric convection on South Tibet summer precipitation isotopologue composition using a combination of in-situ satellite data, and atmospheric general circulation modeling. J. Geophys. Res. Atmos. 120, 3852–3871. https://doi.org/10.1002/2014JD022180.

Hersbach, H., et al., 2018. ERA5 hourly data on single levels from 1979 to present. In: Copernicus Climate Change Service (C3S) Climate Data Store (CDS). https://doi.org/10.24381/cds.adbb2d47.

Huang, L.J., Wen, X.F., 2014. Temporal variations of atmospheric water vapor δD and $\delta^{18}O$ above an arid artificial oasis cropland in the Heihe River Basin. J. Geophys. Res. Atmos. 119 (19) https://doi.org/10.1002/2014JD021891, 11, 456–11, 476.

Jouzel, J., 1986. Isotopes in cloud physics: Multistep and multistage processes, The Terrestrial Environment B. In: Fritz, P., Fontes, J.C. (Eds.), Handbook of Environmental Isotopes Geochemistry, vol. 2. Elsevier, pp. 61–112.

Kleist, D.T., et al., 2009. Introduction of the GSI into the NCPE global data assimilation system. Weather Forecast. 24 (6), 1691–1705. https://doi.org/10.1175/2009WAF2222201.1.

Lai, C.T., et al., 2006. Contributions of evaporation, isotopic non-steady state transpiration and atmospheric mixing on the $\delta18O$ of water vapour in Pacific Northwest coniferous forests. Plant Cell Environ. 29 (1), 77–94. https://doi.org/10.1111/j.1365-3040.2005.01402.x.

Laskar, A.H., et al., 2014. Stable isotopic composition of near surface atmospheric water vapor and rain-vapor interaction in Taipei, Taiwan. J. Hydrol. 519 (B), 2091–2100. https://doi.org/10.1016/j.jhydrol.2014.10.017.

Li, Y.J., et al., 2020. Variations of Stable Isotopic Composition in Atmospheric Water Vapor and their Controlling Factors—a 6-Year Continuous Sampling Study in Nanjing, Eastern China. J. Geophys. Res. Atmos. 125 (22) https://doi.org/10.1029/2019JD031697.

Majoube, M., 1971. Fractionnement en oxygène 18 et en deutérium entre l'eau et sa vapeur. Journal de Chimie Physique et de Physico-Chimie Biologique. 68, 1423–1436. https://doi.org/10.1051/jcp/1971681423.

Merlivat, L., Jouzel, J., 1979. Global climatic interpretation of the deuterium-oxygen-18 relationship for precipitation. J. Geophys. Res. 84 (C8), 5029–5033. https://doi.org/10.1029/JC084iC08p05029.

Risi, C., et al., 2013. Role of continental recycling in intraseasonal variations of continental moisture as deduced from model simulations and water vapor isotopic measurements. Water Resour. Res. 49, 4136–4156. https://doi.org/10.1002/wrcr.20312.

Schmidt, M., et al., 2010. Concentration effects on laser-based delta O-18 and delta H-2 measurements and implications for the calibration of vapour measurements with liquid standards. Rapid Commun. Mass Spectrom. 24 (24), 3553–3561. https://doi.org/10.1002/rcm.4813.

Schoch-Fischer, H., et al., 1984. Hydrometeorological Factors Controlling the Time Variation of D, 18O and 3H in Atmospheric Water Vapour and Precipitation in the Northern Westwind belt. Isotope Hydrology 1983. International Atomic Energy Agency, Vienna, pp. 3–31.

Steen-Larsen, H.C., et al., 2013. Continuous monitoring of summer surface water vapour isotopic composition above the Greenland Ice Sheet. Atmos. Chem. Phys. 13 (1) https://doi.org/10.5194/acpd-13-1399-2013.

Steen-Larsen, H.C., et al., 2014. What controls the isotopic composition of Greenland surface snow? Clim. Past. 10 (1), 377–392. https://doi.org/10.5194/cp-10-377-2014.

Steen-Larsen, H.C., et al., 2017. Evaluating the skills of isotope-enabled general circulation models against in situ atmospheric water vapor isotope observations. J. Geophys. Res. Atmos. 122 https://doi.org/10.1002/2016JD025443.

Stein, A.F., et al., 2015. Potential use of transport and dispersion model ensembles for forecasting applications. Wea. Forecasting. 30, 639–655. https://doi.org/10.1175/WAF-D-14-00153.1.

Stewart, M.K., 1975. Stable isotope fractionation due to evaporation and isotopic-exchange of falling waterdrops - applications to atmospheric processes and evaporation of lakes. J. Geophys. Res. 80 (9), 1133–1146. https://doi.org/10.1029/JC080i009p01133.

Taylor, C.B., 1968. Die isotopenzusammensetzung des atmosphärischen Wasserdampfs in Höhenbereich 500 bis 5000 m über Festland. Doctoral Thesis. 2. Physikalisches Institut der University, Heildelberg, p. 54.

Tian, L.D., et al., 2001. Tibetan Plateau summer monsoon northward extent revealed by measurements of water stable isotopes. J. Geophys. Res. Atmos. 106 (D22) https://doi.org/10.1029/2001jd900186.

Tian, L.D., et al., 2020. Control of seasonal water vapor isotope variations at Lhasa, southern Tibetan Plateau. J. Hydrol. 580 (2020), 124237. https://doi.org/10.1016/j.jhydrol.2019.124237.

Tremoy, G., et al., 2011. Measurements of water vapor isotope ratios with wavelength-scanned cavity ring-down spectroscopy technology: new insights and important caveats for deuterium excess measurements in tropical areas in comparison with isotope-ratio mass spectrometry. Rapid Commun. Mass Sp. 25, 3469–3480. https://doi.org/10.1002/rcm.5252.

Wallace, J., Hobbs, P., 2006. Atmospheric thermodynamics. In: Atmospheric Science: an Introductory Survey, Chap. 3. Academic, San Diego, California, pp. 79–86.

Welp, L.R., et al., 2008. $\delta^{18}O$ of water vapour, evapotranspiration and the sites of leaf water evaporation in a soybean canopy. Plant Cell Environ. 31 (9), 1214–1228. https://doi.org/10.1111/j.1365-3040.2008.01826.x.

Wen, X.F., et al., 2010. Water vapor and precipitation isotope ratios in Beijing, China. J. Geophys. Res. 115 (D1), D01103 https://doi.org/10.1029/2009jd012408.

White, James W.C., Gedzelman, S.D., 1984. The isotopic composition of atmospheric water vapor and the concurrent meteorological conditions. J. Geophys. Res. Atmos. 89 (D3), 4937–4939. https://doi.org/10.1029/JD089iD03p04937.

Worden, J., et al., 2007. 2007. Importance of rain evaporation and continental convection in the tropical water cycle. Nature. 445 (7127), 528–532.

Yao, T.D., et al., 2013. A review of climatic controls on $\delta^{18}O$ in precipitation over the Tibetan Plateau: Observations and simulations. Rev. Geophys. 51 https://doi.org/10.1002/rog.20023.

Yin, C.L., et al., 2008. Temporal variations of $\delta^{18}O$ of atmospheric water vapor at Delingha. Sci. China. Ser. D51, 966–975.

Yu, W.S., et al., 2006. Isotopic composition of atmospheric water vapor before and after the monsoon's end in the Nagqu River Basin. Chin. Sci. Bull. 50 (23), 2755–2760. https://doi.org/10.1360/982005-802.

Yu, W.S., et al., 2015a. Simultaneous monitoring of stable oxygen isotope composition in water vapour and precipitation over the central Tibetan Plateau. Atmos. Chem. Phys. 15 (18) https://doi.org/10.5194/acp-15-10251-2015.

Yu, W., et al., 2015b. Short-term variability in the dates of the Indian monsoon onset and retreat on the southern and northern slopes of the Central Himalayas as determined by precipitation stable isotopes. Clim. Dyn. https://doi.org/10.1007/s00382-015-2829-1.

Zhang, S.C., et al., 2011. Short-term variations of vapor isotope ratios reveal the influence of atmospheric processes. J. Geogr. Sci. 21 (3), 401–416. https://doi.org/10.1007/s11442-011-0853-6.